PNAS
www.pnas.org

Supplementary Information for

Engineering opposite electronic polarization of singlet and triplet states increases the yield of high-energy photoproducts

Nicholas F. Polizzi[1], Ting Jiang[2], David N. Beratan[1,2,3] and Michael J. Therien[2]

[1]Department of Biochemistry Duke University, Durham, North Carolina 27710, United States
[2]Department of Chemistry, Duke University, Durham, North Carolina 27708, United States
[3]Department of Physics, Duke University, Durham, North Carolina 27708, United States

Corresponding authors: David N. Beratan and Michael J. Therien
Email: David.Beratan@duke.edu and Michael.Therien@duke.edu

This PDF file includes:

www.pnas.org/cgi/doi/10.1073/pnas.1901752116

Chemical Synthesis of RuPZn−NDI

RuPZn and RuPZn−NDI in this manuscript were synthesized as the $(PF_6^-)_2$ salts of $RuPZn^{2+}$ and $RuPZn{-}NDI^{2+}$. The synthesis of RuPZn−NDI was accomplished according to Scheme S1. Synthesis of [5-amino-10,20-bis(2,6-bis(3,3-dimethyl-1-butyloxy)phenyl)porphinato]zinc(II) (**3**), *N*-(n-octyl)-naphthalene-1,8-dicarboxyanhydride-4,5-dicarboximide (**4**) and ruthenium(II) (4'-bromo-2,2';6',2"-terpyridine)(2,2';6',2"-terpyridine) bis(hexafluorophosphate) (**6**) were performed as in previous studies (1-3).

Characterization Instrumentation

A 400 MHz Brüker spectrometer was used to obtain NMR spectra for all synthesized compounds. Chemical shifts for ^1H NMR spectra are reported relative to residual proton in deuterated solvent (δ (residual) = 7.26 ppm in $CDCl_3$, δ (residual) = 1.94 ppm in CD_3CN). All J values are reported in Hertz. Reported mass spectra were acquired with a Perspective Voyager DE instrument at the Department of Chemistry in Duke University. Samples were prepared as micromolar solutions in acetone, using HABA (2-(4-hydroxyphenylazo)benzoic acid) as the matrix. Electronic absorption spectra were acquired on a Shimadzu Pharmaspec UV-1700 spectrometer. Cyclic voltammetry and differential pulse voltammetry experiments were performed on a BASi EC Epsilon working station, using an Ag/AgCl (3M NaCl) reference electrode, a Pt wire counter electrode, and a glassy carbon working electrode. The ferrocene/ferrocenium redox couple (0.43 V *vs.* SCE) was used as an internal standard in these experiments.

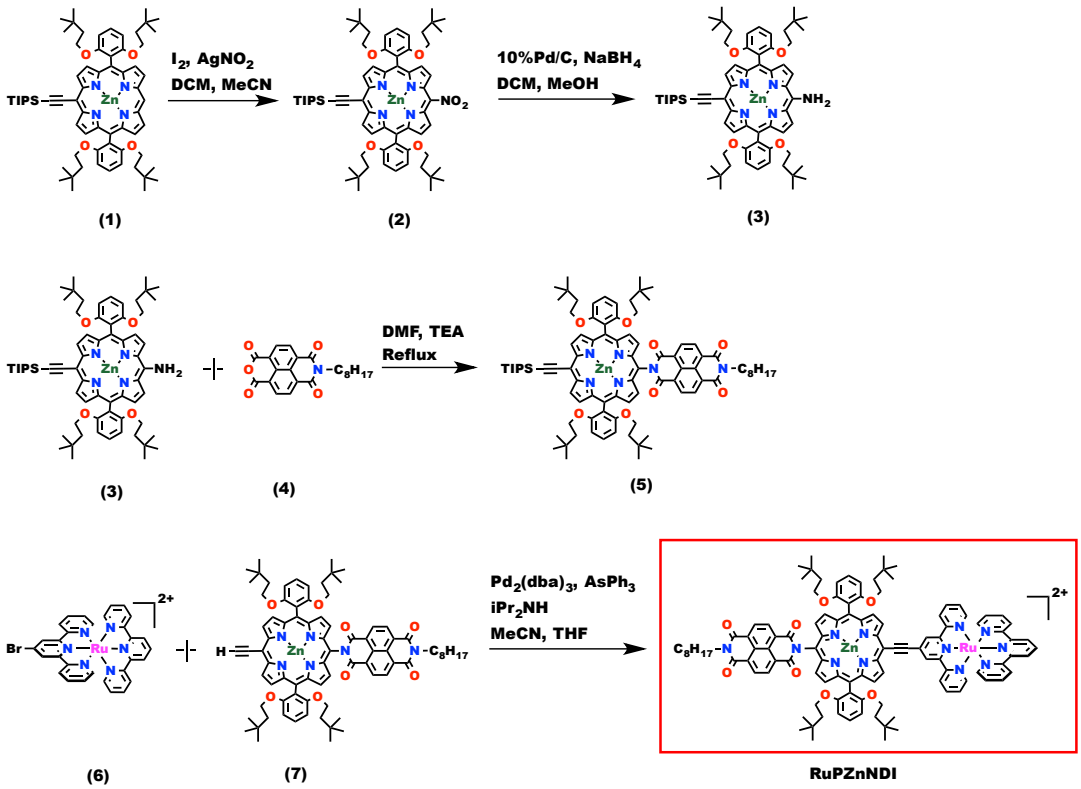

[a] *All ionic compounds have PF_6^- as anions*

Scheme S1. Synthetic route for RuPZn−NDI.

[5-Nitro-15-triisopropylsilylethynyl -10,20-bis(2,6-bis(3,3-dimethyl-1-butyloxy)phenyl)porphinato]zinc(II) (2). A 1000 mL round bottom flask equipped with a stirbar was charged with **1** (250 mg, 0.226 mmol) under Ar. After adding 300 ml DCM and 120 ml MeCN to the flask, the flask was cooled in an ice bath. Iodine (48 mg, 0.189 mmol) dissolved with 30 ml DCM was added. The reaction flask was then shielded with foil. After 5 min, $AgNO_2$ (52.2 mg, 0.339 mmol) in 50 ml MeCN was added dropwise. The reaction was terminated when TLC showed the starting material **1** was completely consumed. Water was added to the reaction mixture and it was extracted with DCM. The solvent was evaporated and the compound was purified by silica gel

chromatography (DCM/Hexane = 4:1). The second band was collected and evaporated to dryness to yield green product (232 mg, 89%).

^{1}H NMR (400 MHz, $CDCl_3$) δ(ppm) 9.69 (d, 2H, J = 4 Hz), 9.21 (d, 2H, J = 4 Hz), 8.90 (d, 2H, J = 4 Hz), 8.86 (d, 2H, J = 4 Hz), 7.71 (t, 2H, J = 8 Hz), 7.00 (d, 4H, J = 8 Hz), 3.91 (t, 8H, J = 8 Hz), 0.82 (t, 8H, J = 8 Hz), 0.32 (s, 36H).

$C_{67}H_{87}N_5O_6SiZn$: m/z=1151.93, MALDI-TOF-MS: m/z = 1152.97 $[\mathbf{2}+H]^+$

[5-Amino-15-triisopropylsilylethynyl -10,20-bis(2,6-bis(3,3-dimethyl-1-butyloxy)phenyl)porphinato]zinc(II) (3). A 250 mL two-neck round bottom flask equipped with a stirbar was charged with **2** (219 mg, 0.190 mmol) under Ar. 70 ml DCM and 70 ml methanol were added. After that, 10% Pd/C (6.5 mg) was added. $NaBH_4$ was added in portions (1eq, 7.16 mg, 0.19 mmol) and stirred for 10 min before adding another portion. When TLC showed the reaction was complete, saturated NH_4Cl was added to neutralize the reaction solution. The product was extracted with DCM. The solvent was evaporated and the compound was purified by silica gel chromatography (DCM). The major band was collected and evaporated to dryness to yield green product (196 mg, 87%).

^{1}H NMR (400 MHz, $CDCl_3$) δ(ppm) 9.36 (d, 2H, J = 4 Hz), 8.65 (d, 2H, J = 4 Hz), 8.27 (d, 2H, J = 4 Hz), 8.13 (d, 2H, J = 4 Hz), 7.68 (t, 2H, J = 8 Hz), 6.99 (d, 4H, J = 8 Hz), 4.99 (br, 2H), 3.94 (m, 8H), 0.99 (t, 8H, J = 8 Hz), 0.38 (s, 36H).

$C_{67}H_{89}N_5O_4SiZn$: m/z= 1121.95, MALDI-TOF-MS: m/z = 1123.12 $[\mathbf{3}+H]^+$

***N*-(n-octyl)-naphthalene-1,8-dicarboxyanhydride-4,5-dicarboximide (4)**. 1,4,5,8-

Naphthalenetetracarboxydianhydride (15.094 g, 0.056 mol) was refluxed under Ar with stirring in 150 ml DMF. Octylamine (9.42 ml, 0.057 mol) in 40 ml DMF was added dropwise. The reaction was terminated after refluxing for 15 h. The reaction was then filtered, and the filtrate was dried. The orange product was recrystallized in DCM (5.73 g, 26.8%).

^{1}H NMR (400 MHz, $CDCl_3$) δ(ppm) 8.82 (s, 4H), 4.20 (t, 2H, J = 8 Hz), 1.74 (m, 2H), 1.2~1.5 (m, 10H), 0.88 (m, 3H).

N-[5-[15-(2-triisopropylsilylethynyl)-10,20-bis(2,6-bis(3,3-dimethyl-1-butyloxy) phenyl)porphinato]zinc(II)-N'-(octyl)naphthylene diimide (5). A 100 mL round-bottom-flask equipped with a stirbar was charged with **3** (180 mg, 0.160 mmol) and **4** (121.7 mg, 0.320 mmol) under Ar. 50 ml dry DMF and 5 ml triethylamine were added. The reaction mixture was refluxed overnight. After cooling to room temperature, the mixture was diluted with chloroform and washed with water. The organic phase was dried with anhydrous Na_2SO_4 and evaporated to dryness. The compound was purified by silica gel chromatography (THF/hexanes = 15:85). The major band was collected and evaporated to dryness to yield green product (104 mg, 43.7%).

^{1}H NMR (400 MHz, $CDCl_3$) δ(ppm) 9.71 (d, 2H, J = 4 Hz), 8.97 (dd, 4H, J_1 = 8 Hz, J_2 = 20 Hz), 8.89 (d, 2H, J = 4 Hz), 8.88 (d, 2H, J = 4 Hz), 8.81 (d, 2H, J = 4 Hz), 7.66 (t, 2H, J = 8 Hz), 6.94 (d, 4H, J = 8 Hz), 4.30 (t, 2H, J = 8 Hz), 3.88 (m, 8H), 1.83 (m, 2H), 1.2~1.5 (m, 10H), 0.91 (t, 8H, J = 8 Hz), 0.36 (s, 36H).

$C_{89}H_{108}N_6O_8SiZn$: m/z= 1480.73, MALDI-TOF-MS: m/z = 1481.81 $[\mathbf{5}+H]^+$

Ruthenium (II) 5-[4'-ethynyl-(2,2';6',2"-terpyridinyl)]-15-(N-(N'-octyl)naphthylene diimide)bis[10,20-bis(3,3-dimethyl-1-butyloxy)phenyl)porphinato]zinc(II)-bis(2,2';6',2"-terpyridine)$^{2+}$ bis-hexafluorophosphate (RuPZn–NDI). Compound **7** derives from the deprotection reaction of **5** in a similar procedure as reported(3). A 100 mL Schlenk flask equipped with a stirbar was charged with **7** (from 104 mg **5**), **6** (98.2 mg, 0.105 mmol), $Pd_2(dba)_3$ (6.4 mg, 0.007 mmol) and $AsPh_3$ (21.44 mg, 0.07 mmol) under Ar. 20 ml THF, 20 ml acetonitrile and 5 ml diisopropylamine were mixed together and added after being degassed by 3 freeze-pump-thaw cycles. The mixture was heated at 60 °C overnight. When the reaction was complete, most of the solvent was removed. A small amount of acetonitrile was added to dissolve the mixture. Saturated ammonium hexafluorophosphate was added to precipitate the product. The crude product was filtered and dried. The compound was then purified by silica gel chromatography (acetonitrile/THF/water/saturated KNO_3 water solution = 60/30/9/1). The brown band was collected and evaporated to 30 ml and saturated ammonium hexafluorophosphate was added to precipitate the product, which was then filtered and dried to give a brown-greenish solid (95 mg, 62%, based on **5**).

^{1}H NMR (400 MHz, CD_3CN) δ(ppm) 10.00 (d, 2H, J = 4 Hz), 9.39 (s, 2 H), 9.11 (d, 2H, J = 4 Hz), 8.99 (d, 2H, J = 4 Hz), 8.89 (s, 4H), 8.77 (d, 4H, J = 8 Hz), 8.71 (d, 2H, J = 4 Hz), 8.51 (d, 2H, J = 8 Hz), 8.45 (t, 1H, J = 8 Hz), 8.04 (t, 2H, J = 8 Hz), 7.95 (t, 2H, J = 8 Hz), 7.78 (t, 2H, J = 8 Hz), 7.55 (d, 2H, J = 8 Hz), 7.41 (d, 2H, J = 8 Hz), 7.22 (dd, 4H, J = 8 Hz), 7.13 (d, 4H, J = 8 Hz), 4.42 (t, 2H, J = 8 Hz), 3.95 (m, 8H), 1.80 (m, 2H), 1.2~1.5 (m, 10H), 0.81 (t, 8H, J = 8 Hz), 0.22 (s, 36H).

$C_{110}H_{108}N_{12}O_8RuZn$: m/z= 1891.68, MALDI-TOF-MS: m/z = 1893.40

[**RuPZn**−**NDI**+H]$^+$, 2037.53 [**RuPZn**−**NDI**+PF_6^-]$^+$

Supplementary Methods

Global analysis of pump-probe data. Globally fitting the data to a discrete number of exponentials is an approximation that assumes discrete absorbing states (4, 5). Due to extensive vibrational relaxation of the molecules described in this report, this approximation is not rigorously upheld. Nevertheless, global fitting provides a measure of the significant time scales of excited state population flow in these systems. The number (n) of exponentials of each fit was determined by convergence of the percentage variance accounted for by the fit, i.e. convergence of [var(data)-var(data-fit(n))]/var(data). The decay-associated difference spectra (DADS) and evolution-associated difference spectra (EADS) are also chirp-free. EADS, which follow a sequential kinetic mechanism, were obtained from the DADS by a linear transformation (4) coded in Matlab. These spectra are given in Fig. S4. The error bars associated with each lifetime represent ± 1 standard deviation as derived from the Jacobian of the non-linear least squares optimum fit. Due to the extensive amount of hot ground-state formation upon $S_0 \rightarrow S_2$ and $S_0 \rightarrow S_1$ excitation of TIPS−ethyne−PZn−NDI, only LDA maps of the data are shown (Fig. S7). The Matlab code used for our data analysis in this report is available upon request.

Chirp-correction procedure. Because the sapphire window and sample cuvette have finite thicknesses, the white light continuum obtains a wavelength-dependent temporal

chirp, despite using all-reflective optics (4-6). We corrected the wavelength-dependent time-zero by collection of the pump-probe transient signal of neat acetonitrile solvent under identical experimental conditions as the molecular experiments. The wavelength-dependent coherent artifact (e.g., stimulated Raman absorption and emission) near time-zero was fit to a Gaussian and its first and second derivatives (6, 7). The extracted time-zeros from these fits were then fit to a linear chirp in the frequency domain. All reported pump-probe data were chirp-corrected by interpolation in the time domain using this linear fit to define the new time-zero at each wavelength.

Treatment of coherent artifact. While the coherent artifact (CA) from acetonitrile is useful for determination of the wavelength-dependent temporal chirp, the CA signal superimposed on the molecular response may hinder data analysis of the molecular response at short time delays (< 1 ps). Scaling and subtracting the CA signal acquired in neat solvent gave unsatisfactory results, derived from the fact that RuPZn and RuPZn−NDI absorb broadly and strongly in the visible region. Explicit fitting of the CA (on top of the molecular response) via a Gaussian function and its first and second derivatives did not satisfactorily reproduce the CA spectra in neat solvent. The following method led to a satisfactory and general solution: To remove the CA component from the TA spectra, we used a smoothing function in Matlab. The (RuPZn, RuPZn−NDI, and TIPS−Ethyne−PZn−NDI) pump-probe spectrum at each time delay less than 2 ps was smoothed in the wavelength domain with a weighting scheme drawn from the CA signal in neat solvent. At each time delay, wavelengths with CA signal in neat solvent greater than 2 standard deviations from the mean were given zero weight in the smoothing

function. In this way, parts of the spectrum preceding the CA are smoothly connected to parts of the spectrum after the CA. This method preserves the noise structure of the data in the time domain, while removing the dominant contributions of the CA signal from the molecular response data.

Lifetime density analysis. Lifetime density analysis (LDA) is a general method for transforming pump-probe transient absorption data into "lifetime space" (7-10). Compared with conventional multi-wavelength global fitting, LDA more appropriately treats transient dynamics with a large degree of vibrational relaxation, appropriate to RuPZn, RuPZn−NDI, and TIPS−Ethyne−PZn−NDI. The kinetic trace at each wavelength is fit with 150 exponentials, with lifetimes uniformly distributed on a log scale. Because this fit is necessarily over-determined, a regularization technique is required for a meaningful solution (7). We utilized lasso-elastic-net regularization (11) as implemented in Matlab to downward bias the number of exponentials with non-zero amplitude. The method minimizes a modified least squares function:

$$\min_{\beta_0,\beta}\left(\frac{1}{2N}\sum_{i=1}^{N}(y_i-\beta_0-x_i^T\beta)^2+\lambda P_\alpha(\beta)\right)$$

where

$$P_\alpha(\beta)=\sum_{j=1}^{p}\left(\frac{1-\alpha}{2}\beta_j^2+\alpha|\beta_j|\right)$$

Here, *N* is the number of data points and *p* the number of fit parameters (amplitudes). Lasso-elastic-net combines lasso regularization with Tikhonov regularization, useful when variables have a large degree of correlation, as they do here (11). For the LDA maps reported here, we used an alpha of 0.9; λ for each wavelength was chosen via cross-validation: 100 different values of λ were distributed on a log scale and used to fit the

data. 10-fold cross-validation was employed to generate the mean squared error (mse) of each λ-dependent fit. We chose the λ that produced a mse 1 standard deviation larger than the minimum mse.

Nanosecond-microsecond pump-probe transient absorption spectroscopy.

Nanosecond transient absorption spectra were acquired utilizing an Edinburgh Instruments LP920 Laser Flash Photolysis Spectrometer and Edinburgh L900 Software. Pump pulses were generated from a Q- switched Nd:YAG laser (Quantel, Brilliant) and a dual-crystal OPO (OPOTEK, Vibrant LDII). The temporal width of the pump pulses was ~5 ns; the energy of the pulses exiting the OPO was controlled using neutral density filters. A Xe flash-lamp was used as a white light probe source, and a CCD array detector enabled acquisition of transient data over the 400 - 800 nm wavelength domain. A PMT detector coupled to an oscilloscope allowed for high-resolution data acquisition in "kinetic mode." Both the LP920 and Opotek OPO are computer interfaced and controlled by the L900 software. Transient spectra reported derive from data acquired over ~20-50 scans. Samples were prepared in 1 cm quartz cells and de-aerated by 3 freeze-pump-thaw-degas cycles prior to excitation. Excited-state lifetimes were calculated via mono-exponential fitting using Origin 9.1 software.

Supplementary Text

<u>RuPZn and RuPZn−NDI excited-state dynamics</u>

The excited ^{1}D* states of RuPZn undergo ultrafast intersystem crossing to a low-lying triplet excited state (^{3}D*) with near unity quantum yield (1, 12); in RuPZn−NDI, ultrafast electron transfer (ET) is also kinetically competent. As S_2 and S_3 share similar dipole moments (Fig. 1B), the electron-transfer (ET) dynamics to NDI initiated from these states are nearly indistinguishable in RuPZn−NDI, bearing credence that the polarizations of these states are key to the dynamics, rather than energetics alone.

Fig. S3 shows a side-by-side comparison of the pump-probe spectra of RuPZn (left column: A, C, E) and RuPZn−NDI (right column: B, D, F) for excitations into the lowest three singlet excited states of each. The transient spectra evinced upon electronic excitation of RuPZn show distinct ground state bleaching signatures at 450 nm, 520 nm, and 640 nm, corresponding the ground-state electronic absorption spectrum of RuPZn (1, 12) (see Fig. 1A). A weak, positive transient absorption is observed between the two bleaches at 520 nm and 640 nm. The strong, broad transient absorption feature in the near-IR (800-1100 nm) is indicative of the RuPZn ^{3}D* state (1, 12), and is evident in the long-time-delay transient absorption spectra of Fig. S3, A, C, and E. Essentially no recovery of the ground state bleach of RuPZn is observed on timescales < 4 ns, and the lifetime of the lowest RuPZn ^{3}D* state is 44 μs in oxygen-free acetonitrile (1, 12). Upon photo-excitation, the RuPZn-localized singlet and triplet excited states of RuPZn−NDI (^{1}D*A and ^{3}D*A, respectively) access two additional decay channels relative to RuPZn: singlet ET to the NDI acceptor (A), (^{1}D*A → ^{1}D$^+$A$^-$), and triplet ET to A (^{3}D*A → ^{3}D$^+$A$^-$). The spectral signatures of the NDI anion (A$^-$, highlighted in purple in Fig. S3) are readily observed at 480 and 610 nm (13, 14). The kinetic traces at these wavelengths show clear rise and decay dynamics, distinct from those of RuPZn (Fig. S4, m-r). Upon

$S_0 \rightarrow S_3$ and $S_0 \rightarrow S_2$ excitation, which polarizes RuPZn electron density toward NDI, a large majority of the excited-state population undergoes slow (>100 ps) triplet ET to NDI (Fig. S3, B and D, Fig. S4, n and p). Contrastingly, $S_0 \rightarrow S_1$ excitation, which polarizes RuPZn electron density away from NDI, induces a majority of the excited-state population to undergo ultrafast (< 1 ps) singlet ET to NDI (Figs. S3F and S4r). The characteristic timescales of these excited-state processes are found via global fitting across the entire 400-1100 nm spectral domain (Fig. S4a-l), as well as via lifetime density analysis (LDA) maps (Fig. S5), single-wavelength fitting (Fig. S1D), bleaching band minimum shift (Fig. 4D), time-resolved emission (Fig. 4E), and the (weak) fluorescence excitation spectrum of RuPZn (Fig. 4A and Fig. S1a-c). These time constants were used to derive the time constant of S_3 to $^1D^+A^-$ one-way ET (1.1 ps), by formulating a system of kinetic equations based on the scheme shown in Fig. 6 and using the experimentally determined $^1D^+A^-$: $^3D^+A^-$ yields as a constraint.

LDA maps

The LDA maps of RuPZn (Fig. S5a-f) are fingerprints of its excited-state dynamics. For instance, a characteristic 20 ps lifetime is attributed to S_1 intersystem crossing into the triplet manifold; this assignment is supported by stimulated emission dynamics and time-resolved fluorescence experiments (Figs. 4D,E). The $^3D^*$ oscillator strength increases on this timescale due to extended conjugation (1, 12). Under different wavelengths of excitation, the maps show a distinct difference in early lifetime (Fig. S5d-f). Two photophysical processes contribute to the early dynamics of RuPZn: intersystem crossing (ISC) to $^3D^*$ and internal conversion (IC) from higher lying singlet states (e.g.

S_3 and S_2) to S_1. The relative quantum yields of emission from S_1, upon excitation into S_3 or S_2, are equal, and 1/3 the magnitude of that observed upon direct excitation into S_1 (Fig. 4A). Rapid internal conversion between from S_3 to S_2 accounts for this data. The pump-probe transient signal in the near-IR upon excitation into S_2 shows an ultrafast rise time of 0.2 ps (Fig. S1C), attributed to intersystem crossing into the triplet manifold. This time constant, along with the relative quantum yield of emission from S_2 compared to that from S_1, determines the internal conversion rate from S_2 to S_1 (0.6 ps). With these rates from S_2, internal conversion from S_3 to S_2 could be calculated with the additional information of the triplet rise time from the pump-probe transient signal in the near-IR (Fig. S1C). The rise time, attributed to the sequential process of internal conversion from S_3 to S_2 followed by intersystem crossing from S_2 to the triplet manifold, determines that IC from S_3 to S_2 is 0.1 ps. Interestingly, the energy gaps between S_3/S_2 and S_2/S_1 states are approximately equal (Fig. 1A, using the red edge of the absorption manifolds), which isolates the effects of electronic polarization on the internal conversion dynamics and minimizes any disparate contributions to these dynamics from the energy gap law (15). These data show that opposite electronic polarizations can not only slow intersystem crossing into the triplet manifold, but can also slow internal conversion between oppositely polarized singlets (here, by a factor of ~ 6 fold).

The LDA maps of RuPZn upon S_3 or S_2 excitation show weak amplitude in the 20 ps time constant region of the map (Fig. S5A,B), as most of the initially populated excited state was funneled into the triplet manifold on the ultrafast time scale. This region describes intersystem crossing from S_1 to the triplet manifold, and shows much stronger amplitude in the map following S_1 excitation (Fig S5C), consistent with the

excitation spectrum of RuPZn (Fig. 4A). Note also the prominent amplitude from stimulated emission between 600 and 700 nm: the negative (blue) amplitude around 650 nm and the positive (yellow) amplitude around 620 nm is indicative of the blue shift of the stimulated emission signal on this time scale (20 ps). This amplitude is much weaker upon S_3/S_2 excitation, which also show ultrafast rise times in the near-IR that are absent upon S_1 excitation (consistent with the singlet wavelength data in Fig. S1C). These LDA maps show that S_1 of RuPZn is afforded a longer lifetime than S_2 and S_3, due to an attenuated rate of intersystem crossing to $^3D^*$.

In contrast to RuPZn, RuPZn−NDI exhibits a large degree of ground state recovery on time scales < 100 ns, with excitation-wavelength-dependent kinetics (Fig. S3). The decay-associated difference spectra (DADS) and evolution-associated difference spectra (EADS) of RuPZn−NDI (Fig. S4) show timescales of singlet ET and charge recombination of 0.8 ps and 2 ps, respectively. These spectra also show timescales of triplet ET (~135 ps) and relaxation of the $^3D^+A^-$ state (> 4 ns). The recombination lifetime of the $^3D^+A^-$ state was characterized via nanosecond pump-probe transient absorption spectroscopy and was found to be 30 ± 1 ns (Fig. S6). LDA maps of RuPZn−NDI (Fig. S5d-f) show that $S_0 \rightarrow S_3$ (j) and $S_0 \rightarrow S_2$ (k) excitation results in kinetics described by longer lifetimes than $S_0 \rightarrow S_1$ (l) excitation. Fig. S5j,k shows large amplitudes for lifetimes near 135 ps and > 4 ns, associated with the formation and relaxation of the $^3D^+A^-$ state. Here, the excited state population of S_3/S_2 is efficiently funneled to the triplet manifold, after which a slower triplet ET takes place. Contrastingly, the LDA map of the dynamics following $S_0 \rightarrow S_1$ excitation shows essentially no amplitude for lifetimes greater than 10 ps, emphasizing the high efficiency

of singlet ET to A from S_1 (Fig. S5l). Excellent LDA fits to the kinetics of RuPZn−NDI are shown at various wavelengths in Fig. S5g-l. Note that the transient signal at 480 nm, indicative of A^-, grows positively due to charge separation and subsequently decays due to charge recombination.

Single-wavelength fitting of RuPZn intersystem crossing

We precisely determined the instrument response function (time zero and Gaussian full-width half maximum) for single wavelength (930 nm) probe by measuring the coherent artifact signal in pure solvent. With this information, we can accurately determine an ultrafast time constant of intersystem crossing in RuPZn following $S_0 \rightarrow S_3$ and $S_0 \rightarrow S_2$ excitation (Fig. S1C). $S_0 \rightarrow S_3$ excitation elicits a 0.3 ps triplet rise time, whereas $S_0 \rightarrow S_2$ excitation elicits a 0.2 ps triplet rise time. Conversely, $S_0 \rightarrow S_1$ excitation shows no ultrafast component; instead, the 20 ps rise time corresponds to the lifetime of the S_1 state.

Fluorescence excitation spectrum of RuPZn

If internal conversion from high-lying singlet states to the emitting state S_1 occurred with unit quantum yield, the RuPZn excitation spectrum (Fig. 4A, black) should be identical to its electronic absorption spectrum (Fig. 4A, gray). Comparison of the fluorescence excitation spectrum and electronic absorption spectrum shows that the $S_0 \rightarrow S_3$ and $S_0 \rightarrow S_2$ manifolds of the excitation spectrum are attenuated relative to the absorption spectrum. Relative emission quantum yields were calculated from the

excitation spectrum by dividing the emission intensity at 710 nm by the absorption at the excitation wavelength.

Bleaching band minimum shift of RuPZn

The $S_0 \rightarrow S_1$ bleaching band of RuPZn shows a dynamic blue shift upon excitation of its red edge at 650 nm (Fig. 4D). RuPZn is only very weakly emissive, such that its stimulated emission signal in pump-probe experiments is weak. Nevertheless, the time scale upon which the bleaching band blue shifts can be used to deduce the stimulated emission—and thus S_1 state—lifetime. The $S_0 \rightarrow S_1$ bleaching band of the transient spectra of RuPZn, in wavenumber, was fit to a Gaussian function with an offset (Fig. 4D). The band minimum is defined as the center of the Gaussian fit. The function plotted is the difference in the band minimum at each time-delay minus the band minimum at long-time-delay. The minima are normalized by the difference between the initial and long-time-delay bleaching band minimum values. The fit shows two timescales of blue shifting of the bleaching band: The fastest (0.8 ps) is due to solvational dynamics in acetonitrile, the 20 ps time constant is attributed to the S_1 state lifetime. These assignments are supported by streak-scope measurements of RuPZn fluorescence (Fig. 4E).

TIPS−ethyne−PZn−NDI excited-state dynamics

As a control experiment, we investigated the excited-state dynamics of TIPS−ethyne−PZn−NDI upon excitation into its PZn-localized S_2 and S_1 singlet excited

states (Fig. S7). Fig. S7a,b shows pump-probe data for $S_0 \rightarrow S_2$ excitation with a 400 nm pump pulse (a) and $S_0 \rightarrow S_1$ excitation with a 620 nm pump pulse (b) in acetonitrile solvent. Charge separation occurs in both cases in < 300 fs, evidenced by the spectral signatures of the NDI anion (480 nm, 610 nm) and PZn cation (680-720 nm) at early time delays. Fast charge recombination to the S_0 electronic ground state populates vibrationally hot sublevels (evident at ΔA = 450 nm(16)), and is followed by thermal cooling. The LDA maps of Fig. S7c-d display lifetime "band bending," especially near 450 nm, indicative of vibrational cooling in the hot ground-state manifold. Charge recombination after excitation into S_2 produces a larger degree of non-thermalized ground states, as expected from an initially prepared singlet state with excess energy. Positive (yellow) amplitude at 1.1 ps lifetime denotes the charge recombination process; negative (purple) amplitude < 1 ps lifetime denotes charge separation. Fig. S7c-d shows that no significant changes to the ET dynamics occur in TIPS−ethyne−PZn−NDI upon excitation into S_2 vs. S_1, save for a larger degree of hot ground state formation upon charge recombination from the charge-separated state populated via S_2. Excellent LDA fits to the kinetics of TIPS−ethyne−PZn−NDI are shown at various wavelengths in Fig. S7e-f. These experiments emphasize that the disparate yields of ET products following $S_0 \rightarrow S_3$ and $S_0 \rightarrow S_1$ of RuPZn−NDI (Fig. 3 of the main text) are integrally tied to the supermolecular photophysics of the donor RuPZn.

Hyperpolarizability spectrum of RuPZn

The hyperpolarizability (β_λ) spectrum (Fig. 1B) was calculated from a fit to measured β_λ values at 1300 nm, 1024 nm, and 800 nm incident irradiation (3). We fit these points to a two-level model of the hyperpolarizability (17-20):

$$\beta_\lambda(E_{\mathrm{inc}}) = \sum_{k=1}^{3} \frac{a_k \Delta E_k^2}{(\Delta E_k^2 - E_{\mathrm{inc}}^2 + i\Gamma)(\Delta E_k^2 - (2E_{\mathrm{inc}})^2 + i\Gamma)}$$

where ΔE_k is the energy (in eV) of the *k*-th singlet excited state of RuPZn. The $i\Gamma$ term (We used $\Gamma = 0.07$ eV for the fit.) assures the hyperpolarizability does not diverge at one- and two-photon resonance energies. With 3 equations and 3 unknowns (a_k), the solution is uniquely determined. The resulting β_λ spectrum is the real part of the solution to these equations, and accurately predicts the hyperpolarizability at 1500 nm incident wavelength (500 x 10^{-30} esu) (19). For a more rigorous 3-level treatment of the hyperpolarizability of RuPZn, see ref (19).

Excitation wavelength selectivity at 400 nm:

The extinction coefficient of RuPZn at 400 nm is 40,000 $M^{-1}cm^{-1}$ (ref. (3)), whereas that of NDI is < 500 $M^{-1}cm^{-1}$ (13). This leads to an excitation selectivity ratio at 400 nm of greater than 80:1 (RuPZn : NDI). Consequently, the dynamics evinced from 400 nm excitation of RuPZn−NDI can be safely attributed to selective RuPZn-localized $S_0 \rightarrow S_3$ excitation. Moreover, the dynamics evinced from $S_0 \rightarrow S_3$ excitation of RuPZn−NDI track that of $S_0 \rightarrow S_2$ excitation, where the absorbance of NDI (at 532 nm) is essentially zero.

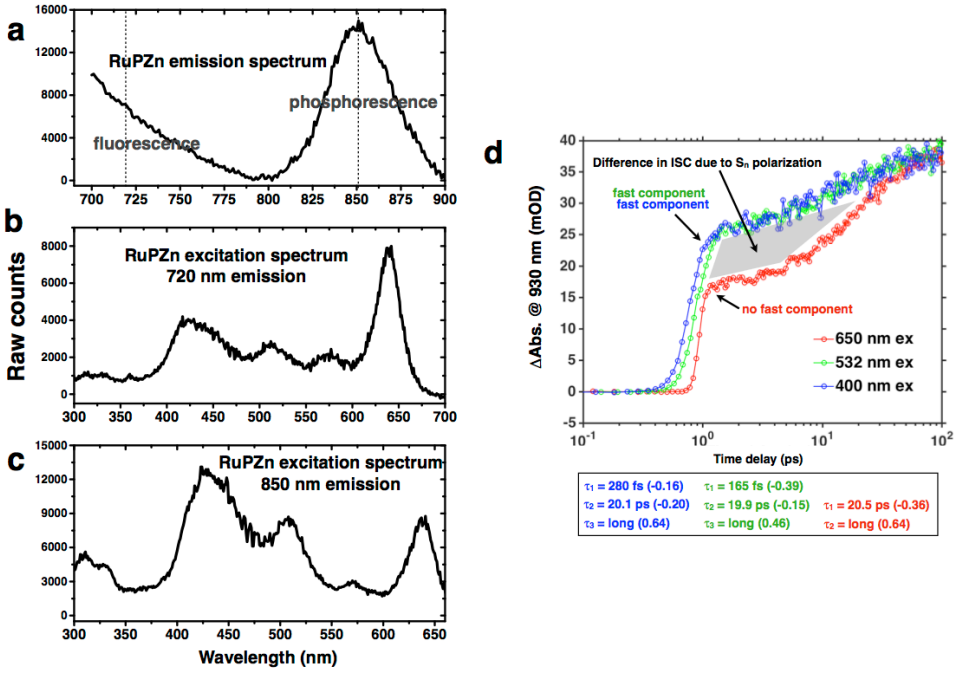

Figure S1 | Intersystem crossing of RuPZn. **a-c,** room-temperature emission and excitation spectra of RuPZn in acetonitrile solvent. **a,** Weak emission bands associated with fluorescence from ^{1}D* (< 780 nm) and phosphorescence from ^{3}D* of RuPZn. **b**, Excitation spectrum monitoring ^{1}D* fluorescence at 720 nm. **c**, Excitation spectrum monitoring ^{3}D* phosphorescence at 850 nm. All spectra are corrected for wavelength-dependent instrument detection sensitivity. The sample was freeze-pump-thaw-degassed three times. **d**, Pump-probe traces of RuPZn in acetonitrile at 930 nm probe for $S_0 \rightarrow S_3$ (blue), $S_0 \rightarrow S_2$ (green), and $S_0 \rightarrow S_1$ (red) excitation. Note that these traces are not chirp-corrected and are scaled to match at 100 ps time delay. The lower box contains the exponential fits (and relative amplitudes) of each trace.

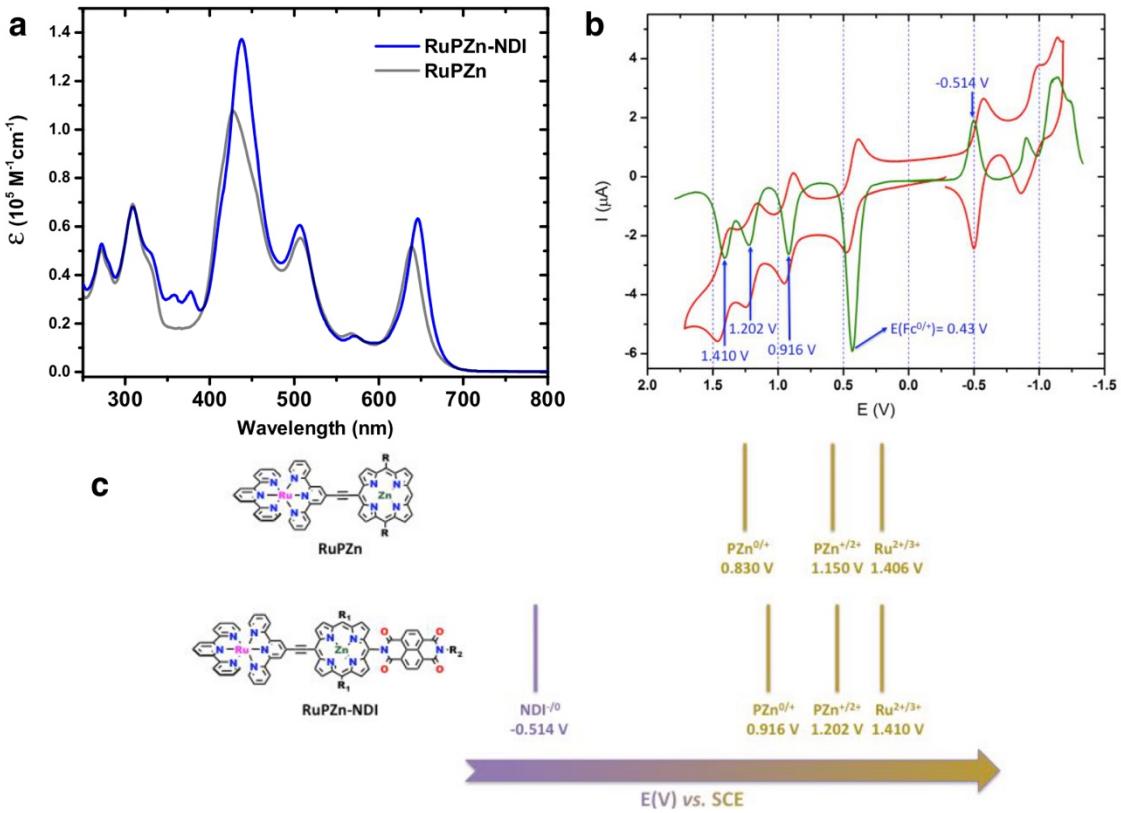

Figure S2 | Optical and potentiometric properties of RuPZn-NDI. **a,** Electronic absorption spectra of RuPZn−NDI and RuPZn in acetonitrile solvent. Blue peaks at 360 nm and 380 nm are characteristic absorptive signatures of NDI. **b**, Potentiometric data of RuPZn−NDI (*vs.* SCE) in 0.1 M $TBAPF_6$/acetonitrile electrolyte/solvent system. Red line represents data from cyclic voltammetry. Green line represents data from differential pulse voltammetry. **c**, Redox potentials (vs. SCE) of RuPZn (upper row) and RuPZn−NDI (bottom row) in 0.1 M $TBAPF_6$/acetonitrile electrolyte/solvent.

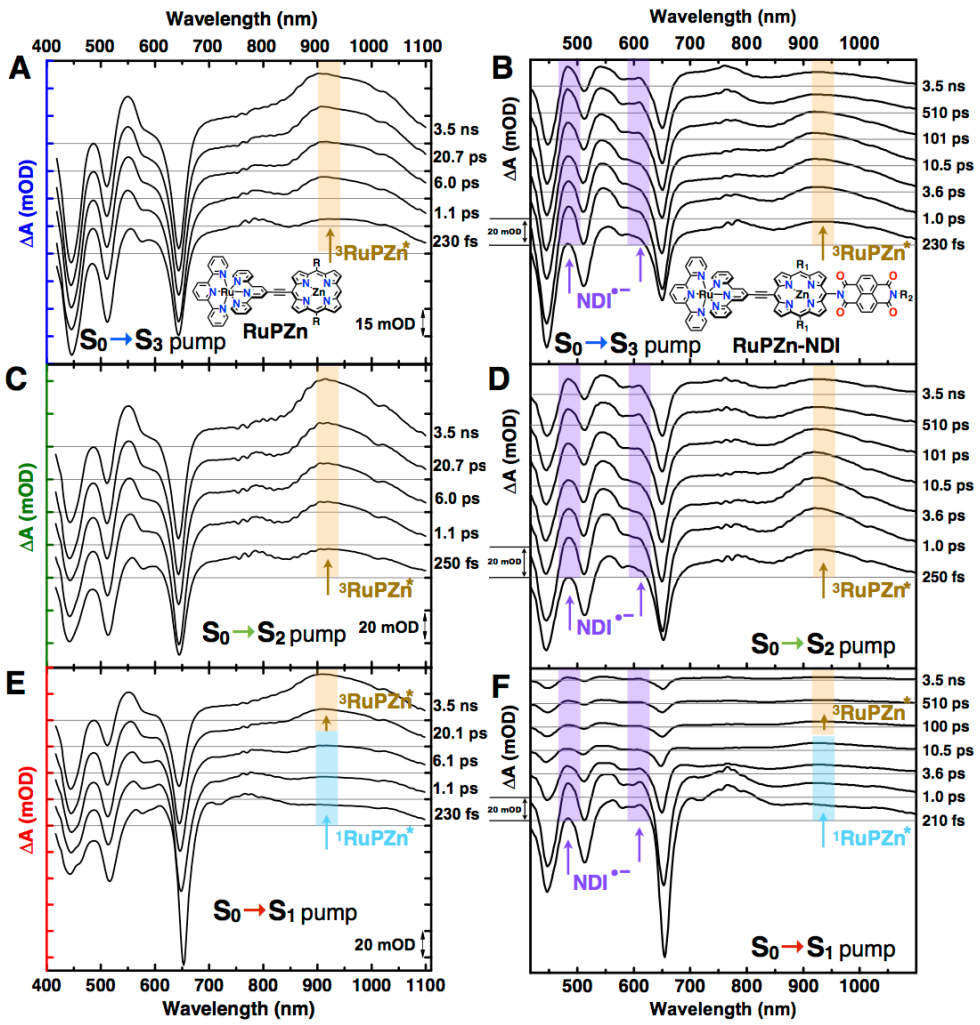

Figure S3 | Transient absorption of RuPZn and RuPZn-NDI. Chirp-corrected pump-probe transient absorption spectra at representative time delays of RuPZn (left) and RuPZn−NDI (right) for excitation into S_3 (**A**, **B**), S_2 (**C**, **D**), and S_1 (**E**, **F**), via a narrow-band (± 5 nm) pump pulse centered at 400 nm, 532 nm, and 650 nm, respectively. The time delay between pump and probe pulses associated with each spectrum is shown to the right of each plot. The constant ΔmOD offset (15 or 20 mOD) between spectra in each plot is shown with doubled-sided arrows. Brown bands highlight the ^{3}RuPZn* (^{3}D* in the main text) triplet absorbance; blue band in (**E**, **F**) denotes the ^{1}RuPZn* (^{1}D* in the main text) singlet absorbance; purple bands in (**B**, **D**, and **F**) denote NDI^- anion

absorbances. Experimental conditions: Magic angle polarization, T= 21 °C, pump fluence = 990 μJ/cm^2 (λ_{ex} = 400 nm), 745 μJ/cm^2 (λ_{ex} = 532 nm), 610 μJ/cm^2 (λ_{ex} = 650 nm). These fluences achieve identical photon densities for each excitation wavelength. R = R_1 = 2',6'-bis(3,3-dimethyl-1-butyloxy)phenyl , R_2 = octyl.

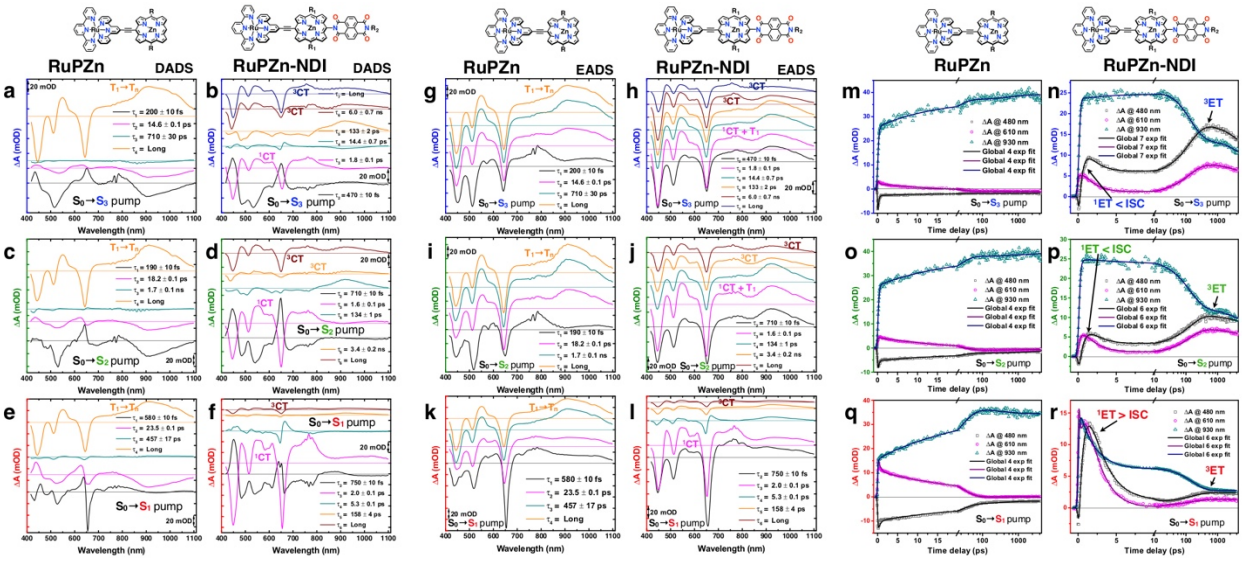

Figure S4 | Global, multi-exponential fits of the pump-probe data in acetonitrile. a-f, Decay-associated difference spectra (DADS) of RuPZn (left column) and RuPZn−NDI (right column). DADS labels show the predominant excited-state character. (^{1}CT and ^{3}CT are $^1D^+A^-$ $^3D^+A^-$ in the main text, respectively.) **g-l**, Evolution-associated difference spectra (EADS) of RuPZn (left column) and RuPZn−NDI (right column). **m-r**, kinetic traces with associated global fits. **a, b**, **g, h, m, and n**, $S_0 \rightarrow S_3$, **c, d**, **i, j, o**, and **p**, $S_0 \rightarrow S_2$, **e, f, k, l, q,** and **r**, $S_0 \rightarrow S_1$ excitation. The ΔmOD difference (15 or 20 mOD) between tic-marks in each plot is shown with doubled-sided arrows. The ΔmOD = 0 line of each spectrum is drawn in the same (but fainter) color. The lifetimes associated with each spectrum are labeled in the inset. Long = constant offset spectrum, also known as an

infinite lifetime. (Note that the DADS and EADS associated with the fastest lifetime (τ_1 ≈ 80 fs) in (**b**, **d**, and **f**) is not shown for clarity. This fast DADS/EADS is likely associated with artifacts due to imperfect time-zero corrections.) The electron-transfer (ET) kinetics of RuPZn−NDI, i.e., fast singlet and slow triplet ET (^{1}ET and ^{3}ET, respectively) to NDI, are labeled with arrows.

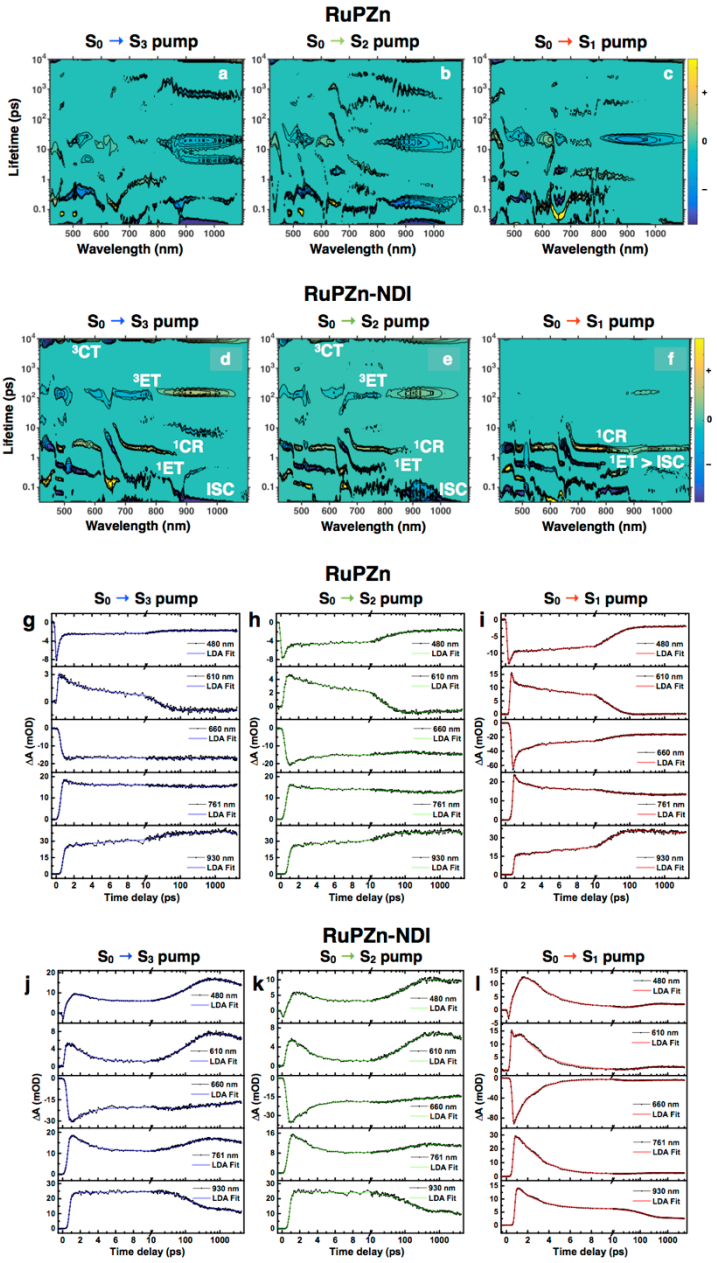

Figure S5 | Lifetime density analysis (LDA) maps of the pump-probe transient dynamics of RuPZn and RuPZn-NDI. **a-c**, sub-100 fs – 10^4 ps LDA maps shown for RuPZn pumped into (**a**) S_3 (400 nm), (**b**) S_2 (532 nm), and (**c**) S_1 (650 nm). Yellow shading denotes positive amplitude and blue shading denotes negative amplitude associated with the corresponding ordinate lifetime. Note that infinite lifetime amplitudes are not shown, although these are substantial due to the long-lived ^{3}D* state of RuPZn.

d-f, sub-100 fs – 10^4 ps LDA maps shown for RuPZn-NDI pumped into (**a**) S_3 (400 nm), (**b**) S_2 (532 nm), and (**c**) S_1 (650 nm). **g-i**, LDA fits to the pump probe data of RuPZn at indicated wavelengths. **j-l**, LDA fits to the pump probe data of RuPZn-NDI at indicated wavelengths. White labels correspond to the dominant kinetic process at these lifetimes. ISC = intersystem crossing, ^{1}ET = singlet electron transfer, ^{1}CR = singlet charge recombination, ^{3}ET = triplet electron transfer, ^{3}CT = triplet charge-transfer state. Contour lines in **a-f** lie along 5%, 15%, 30%, 45%, 60%, 75%, and 90% of the total LDA amplitude.

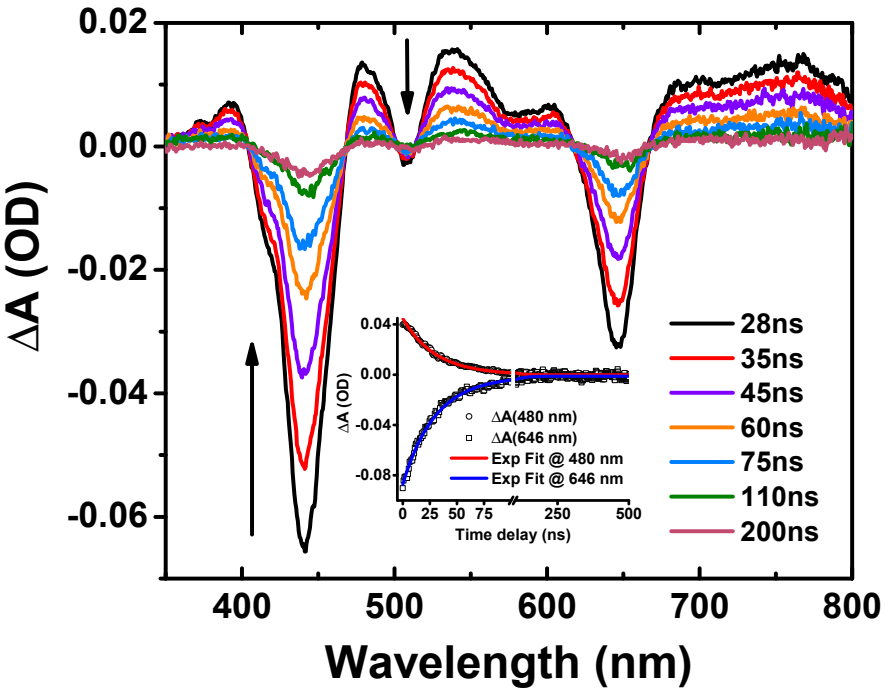

Figure S6 | Nanosecond pump-probe transient absorption spectra of RuPZn−NDI in acetonitrile. Dynamics evinced upon $S_0 \rightarrow S_2$ excitation of RuPZn–NDI via a pump pulse centered at 515 nm. Arrows point in the direction of decrease of the pump-probe signal amplitude. The inset shows kinetics at representative wavelengths overlaid with a global,

single-exponential fit (τ_{CR} = 30 ± 1 ns). The sample was freeze-pump-thaw-degassed three times.

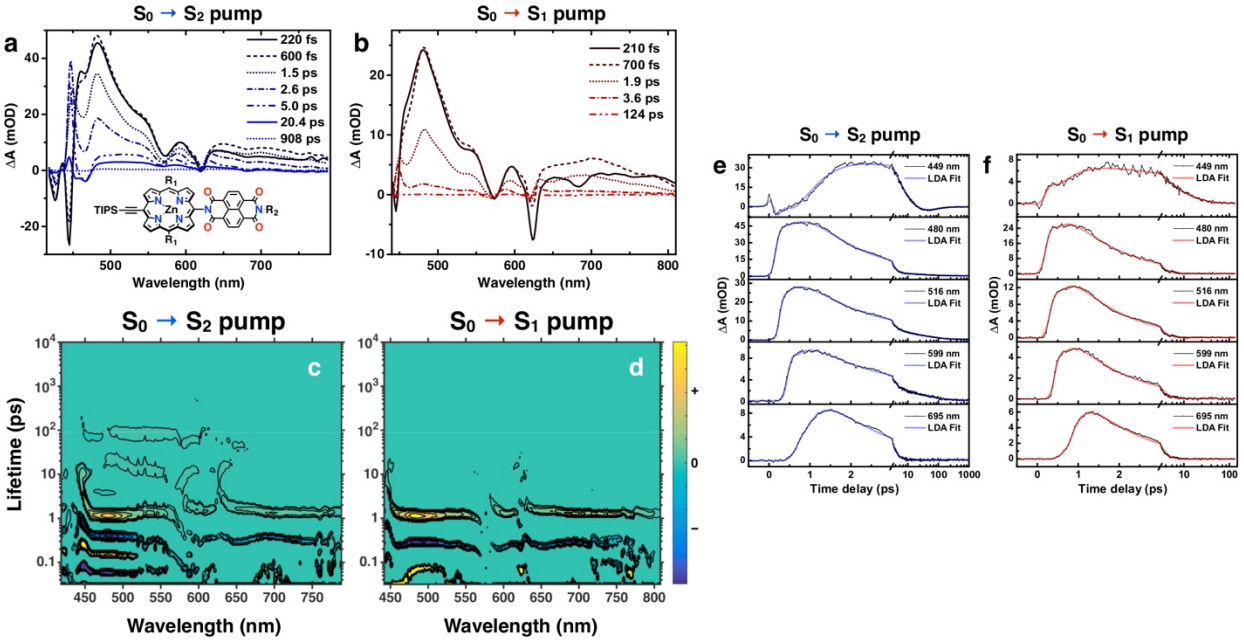

Figure S7 | Transient absorption of TIPS−Ethyne−PZn−NDI. a, b, Chirp-corrected pump-probe transient absorption spectra at representative time delays of TIPS−Ethyne−PZn−NDI for (**a**) $S_0 \rightarrow S_2$ (400 nm) excitation, and (**b**) $S_0 \rightarrow S_1$ (620 nm) excitation. Experimental conditions: Magic angle polarization, T= 21 °C, pump fluence = 990 μJ/cm^2 (λ_{ex} = 400 nm), 590 μJ/cm^2 (λ_{ex} = 620 nm). R_1 = 2',6'-bis(3,3-dimethyl-1-butyloxy)phenyl , R_2 = octyl. **c, d**, Lifetime density analysis (LDA) maps of the pump-probe transient dynamics of TIPS−Ethyne−PZn−NDI upon excitation into (**c**) S_2 (400 nm) and (**d**) S_1 (620 nm). Yellow shading denotes positive amplitude and blue shading denotes negative amplitude associated with the corresponding ordinate lifetime. Contour lines lie along 1%, 5%, 15%, 30%, 45%, 60%, 75%, and 90% of the total LDA

amplitude. **e, f**, Pump-probe transient signals of TIPS−Ethyne−PZn−NDI in acetonitrile at various wavelengths, with overlaid fits from lifetime density analysis (LDA).

References:

1. Duncan TV, Ishizuka T, & Therien MJ (2007) Molecular engineering of intensely near-infrared absorbing excited states in highly conjugated oligo(porphinato)zinc−(polypyridyl)metal(II) supermolecules. *J. Am. Chem. Soc.* 129:9691-9703.
2. Redmore NP, Rubtsov IV, & Therien MJ (2002) Synthesis, excited-state dynamics, and reactivity of a directly-linked pyromellitimide−(porphinato)zinc(II) complex. *Inorg. Chem.* 41:566-570.
3. Uyeda HT*, et al.* (2002) Unusual frequency dispersion effects of the nonlinear optical response in highly conjugated (polypyridyl)metal−(porphinato)zinc(II) chromophores. *J. Am. Chem. Soc.* 124:13806-13813.
4. van Stokkum IHM, Larsen DS, & van Grondelle R (2004) Global and target analysis of time-resolved spectra. *BBA-Bioenergetics* 1657:82-104.
5. Ruckebusch C, Sliwa M, Pernot P, de Juan A, & Tauler R (2012) Comprehensive data analysis of femtosecond transient absorption spectra: A review. *J. Photochem. Photobiol. C* 13:1-27.
6. Kovalenko SA, Dobryakov AL, Ruthmann J, & Ernsting NP (1999) Femtosecond spectroscopy of condensed phases with chirped supercontinuum probing. *Phys. Rev. A* 59:2369-2384.

7. Slavov C, Hartmann H, & Wachtveitl J (2015) Implementation and evaluation of data analysis strategies for time-resolved optical spectroscopy. *Anal. Chem.* 87:2328-2336.

8. Croce R, Müller MG, Bassi R, & Holzwarth AR (2001) Carotenoid-to-chlorophyll energy transfer in recombinant major light-harvesting complex (LHCII) of higher plants. I. Femtosecond transient absorption measurements. *Biophys. J.* 80:901-915.

9. Holzwarth AR*, et al.* (2006) Kinetics and mechanism of electron transfer in intact photosystem II and in the isolated reaction center: Pheophytin is the primary electron acceptor. *Proc. Natl. Acad. Sci. USA* 103:6895-6900.

10. Müller MG*, et al.* (2010) Singlet energy dissipation in the photosystem II light-harvesting complex does not involve energy transfer to carotenoids. *ChemPhysChem* 11:1289-1296.

11. Zou H & Hastie T (2005) Regularization and variable selection via the elastic net. *J. Roy. Stat. Soc. Ser. B. (Stat. Method.)* 67:301-320.

12. Duncan TV, Rubtsov IV, Uyeda HT, & Therien MJ (2004) Highly conjugated (polypyridyl)metal−(porphinato)zinc(II) compounds: Long-lived, high osscillator strength, excited-state absorbers having exceptional spectral coverage of the near-infrared. *J. Am. Chem. Soc.* 126:9474-9475.

13. Gosztola D, Niemczyk MP, Svec W, Lukas AS, & Wasielewski MR (2000) Excited doublet states of electrochemically generated aromatic imide and diimide radical anions. *J. Phys. Chem. A* 104:6545-6551.

14. Redmore NP, Rubtsov IV, & Therien MJ (2003) Synthesis, electronic structure, and electron transfer dynamics of (aryl)ethynyl-bridged donor−acceptor systems. *J. Am. Chem. Soc.* 125:8769-8778.

15. Englman R & Jortner J (1970) The energy gap law for radiationless transitions in large molecules. *Mol. Phys.* 18:145-164.

16. Petersson J, Eklund M, Davidsson J, & Hammarström L (2010) Ultrafast electron transfer dynamics of a Zn(II)porphyrin−viologen complex revisited: S_2 vs S_1 reactions and survival of excess excitation energy. *J. Phys. Chem. B* 114:14329-14338.

17. Kanis DR, Ratner MA, & Marks TJ (1994) Design and construction of molecular assemblies with large second-order optical nonlinearities. Quantum chemical aspects. *Chem. Rev.* 94:195-242.

18. Priyadarshy S, Therien MJ, & Beratan DN (1996) Acetylenyl-linked, porphyrin-bridged, donor−acceptor molecules: A theoretical analysis of the molecular first hyperpolarizability in highly conjugated push−pull chromophore structures. *J. Am. Chem. Soc.* 118:1504-1510.

19. Hu X*, et al.* (2010) Predicting the frequency dispersion of electronic hyperpolarizabilities on the basis of absorption data and Thomas−Kuhn sum rules. *J. Phys. Chem. C* 114:2349-2359.

20. Jiang N*, et al.* (2012) Design of coupled porphyrin chromophores with unusually large hyperpolarizabilities. *J. Phys. Chem. C* 116:9724-9733.